Generalized sweep-stick mechanism of inertial-particle clustering in turbulence

Sunao Oka* and Susumu Goto†
Graduate School of Engineering Science, Osaka University, 1-3 Machikaneyama, Toyonaka, Osaka 560-8531 Japan

(Received 31 August 2020; accepted 26 February 2021; published 8 April 2021)

Inertial particles, i.e., small heavy particles, can inhomogeneously distribute and form clusters even in statistically homogeneous turbulence. When the Reynolds number of turbulence is sufficiently high so that coherent structures with various length and time scales coexist, particles form clusters by the action of the coherent structures when the particle velocity relaxation time is in the inertial-range time scales. In general, thus formed clusters are larger for larger Stokes numbers (the nondimensional relaxation time). We propose a method to objectively describe the particle cluster created by the action of coherent structures in the inertial range. For this purpose, we generalize the sweep-stick mechanism [S. Goto and J. C. Vassilicos, Phys. Rev. Lett. **100**, 054503 (2008)] to express two-dimensional sheetlike clusters in terms of the coarse-grained acceleration field of turbulence. The generalized mechanism also predicts the thickness of the clusters, which depends on the particle relaxation time, the magnitude of acceleration gradients, and the lifetime of coherent flow structures. The direct numerical simulations of fully developed turbulence in a periodic cube with the Taylor-length Reynolds number being about 740 support the proposed mechanism.

DOI: 10.1103/PhysRevFluids.6.044605

I. INTRODUCTION

The transport phenomena of particles in turbulence are fundamental. When the particles are so small that their inertia may be negligible, the classical theories [1,2] predict how turbulence diffuses the centroid of particle blobs and enlarges the relative distance between the particles in the blobs. However, the effects of the inertia (i.e., size and density effects) of particles are not negligible in general. The developments of numerical environments now enable us to conduct numerical simulations of finite-size spherical [3–15], spheroidal [16–18], and fiberlike [19,20] particles in turbulence. Nevertheless, even without the size effects, particle transports in turbulence are nontrivial and worth studying. In particular, when particles are small but their mass density is much larger than fluid, particles distribute inhomogeneously to form clusters even in homogeneous turbulence. This phenomenon, which is sometimes called the preferential concentration, was discovered in the last century [21–23], and several mechanisms were proposed to explain particle clustering in turbulent flows (see the reviews [24,25] and references therein). Although the most classical mechanism is the centrifugal effect of coherent vortices [21], it is basically valid for particles with small inertia, and other mechanisms [26–28] were proposed to describe the condition of the clustering of particles with large inertia. Furthermore, Bec and his colleagues [29–31] developed a general theory of the particle clustering by the dissipative dynamical system approach. We emphasize that particle

*s_oka@fm.me.es.osaka-u.ac.jp
†goto@me.es.osaka-u.ac.jp

clustering is not only scientifically interesting but also important in natural and industrial flows. For example, since the clustering of particles enhances their collisions [32,33] and affects their terminal velocity [34,35], it has non-negligible effects on the droplet growth in cloud turbulence [36,37]. Other systems in which the particle clustering plays a role are given in the reviews [24,25,38].

In the present study, we focus on the clustering of small heavy particles, which we call inertial particles, by the action of coherent structures in statistically homogeneous isotropic turbulence. When the Reynolds number of turbulence is low (say, the Taylor-length Reynolds number R_λ is smaller than 100) there is no hierarchical structure of turbulent eddies. In such a case, coherent vortices at the Kolmogorov length scale make particles form clusters only when the velocity relaxation time τ_p [see (4) in Sec. II A for the definition] of particles is comparable with the characteristic time scale of turbulence [23,34]. In other words, particle clustering due to the centrifugal effects is most pronounced when the Stokes number is approximately 1 in low-Reynolds number turbulence. In the present study, we adopt the Kolmogorov time τ_η [$= (\nu/\epsilon)^{1/2}$, where ϵ is the mean energy dissipation rate of turbulence and ν is the kinematic viscosity of fluid] as the characteristic time scale of turbulence to define the Stokes number:

$$\mathrm{St} = \tau_p/\tau_\eta. \tag{1}$$

The Stokes-number dependence of particle clustering in low-Reynolds number turbulence is explained as follows. When $\mathrm{St} \ll 1$, an inertial particle behaves like a fluid particle, and therefore particles cannot form clusters because of the incompressibility of the fluid. On the other hand, when $\mathrm{St} \gg 1$, particle motions are almost independent of the flow, and therefore they do not cluster by the action of the coherent vortices, although another mechanism [26–28] can lead to the clustering of particles with large St. In contrast, in the intermediate case, i.e., when $\mathrm{St} \approx 1$, particles are swept out from the single-scale (i.e., the Kolmogorov-length) coherent vortices and accumulate in low-vorticity high-strain regions to form clusters [21,34].

If the Reynolds number is high enough, however, inertial particles with $\mathrm{St} \gg 1$ can form clusters by the action of coherent structures in inertial-range length scales and the cluster size depends on St [35,39–41]. For example, Fig. 1 (see the next section and Appendix A for more details) shows the spatial distribution of particles with $\mathrm{St} = 1.3$, 5.0, and 40 in turbulence at $R_\lambda = 740$. It is clear that the particles form clusters even when $\mathrm{St} \gg 1$ and the clusters are larger for larger St. We can explain these observations in terms of the centrifugal effects of coherent vortices with various sizes. High Reynolds number turbulence is composed of the hierarchy of coherent vortices with different length and time scales [42], and the particles are swept out from the vortices whose turnover time is comparable with τ_p. Since larger vortices swirl with a longer turnover time, this mechanism well explains, at least qualitatively, the observations in Fig. 1. It also explains the reason why particles with τ_p in the range $\tau_\eta \lesssim \tau_p \lesssim \mathcal{T}$ may cluster, where $\mathcal{T}$, the integral time, denotes the turnover time of the largest eddies.

The above mechanism in terms of the centrifugal effects of coherent eddies enables us to describe the particle clusters in developed turbulence in terms of flow information. More concretely, we may describe them by low-vorticity high-strain regions at the appropriate length scale depending on τ_p. In fact, Ref. [39] showed that the voids of particles coincide with the regions where the coarse-grained enstrophy is larger than a threshold. However, since we have to choose a threshold, we cannot identify the voids or clusters of particles in an objective manner. The main purpose of the present study is to develop the method to objectively identify, by using the information of turbulent velocity field, the clusters (Fig. 1) of particles with τ_p in the inertial time scales.

In several studies [43–50], the fluid acceleration plays a key role in the description of inertial particle motions. In our previous study [45], we proposed the sweep-stick mechanism (SSM), which predicts that particles accumulate on surfaces $\mathcal{A}$ (see Sec. III A) defined in terms of the fluid acceleration. The SSM is a parameter-free theory and it can predict the clusters of particles with $\mathrm{St} \approx 1$. In fact, for low-Reynolds number turbulence ($R_\lambda \lesssim 150$), it was shown by experiments [51] and by the direct numerical simulations (DNS) of finite-size particles [13] that the SSM explains the preferential locations of particles of $\mathrm{St} \approx 1$. Although an extension to larger St was suggested

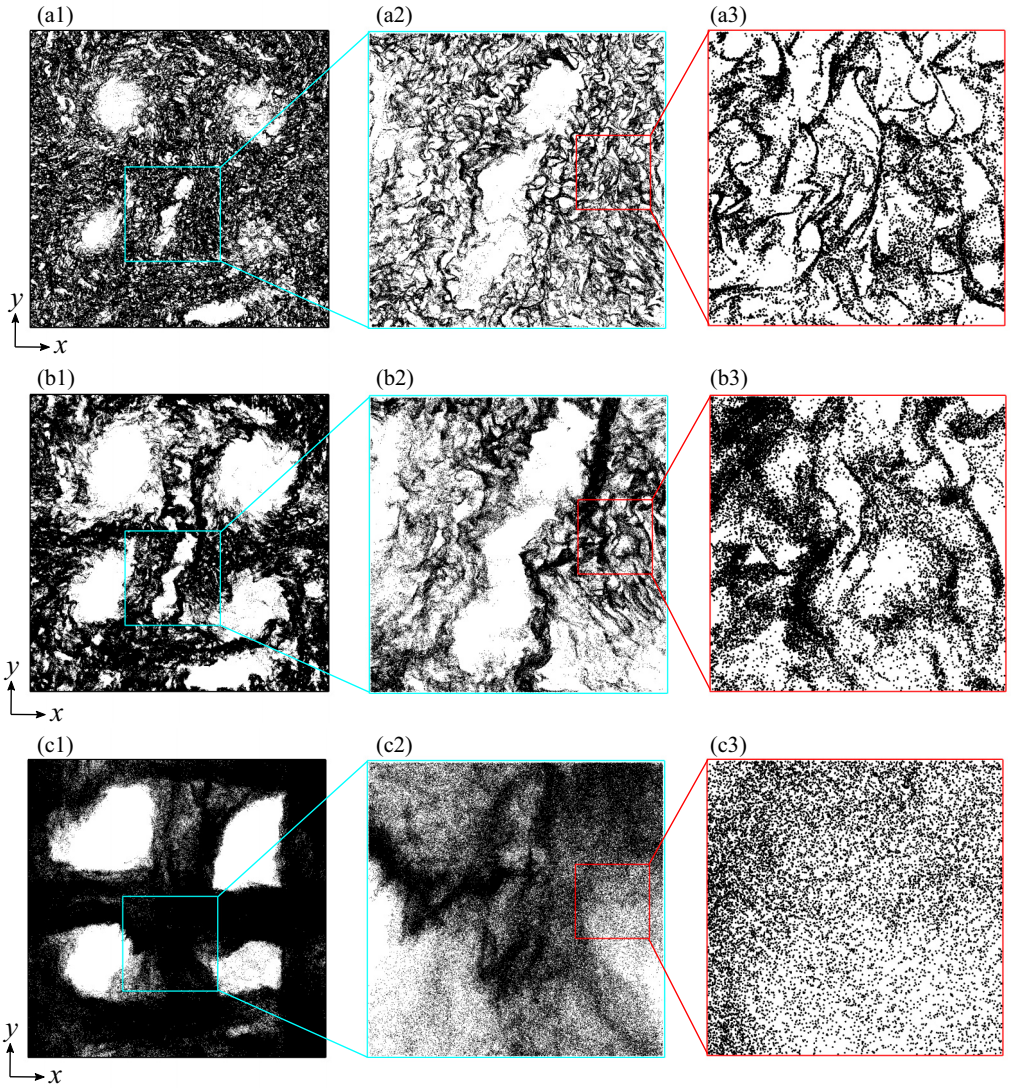

FIG. 1. Spatial distribution of inertial particles within a thin layer (width 10η) for three different Stokes numbers: (a1)–(a3) St = 1.3, (b1)–(b3) 5.0, and (c1)–(c3) 40. Panels (a2),(b2),(c2) and (a3),(b3),(c3) are the magnifications of (a1),(b1),(c1). The sides of the panels are (a1),(b1),(c1) $5.5\mathcal{L} = 4400\eta$, (a2),(b2),(c2) $1.8\mathcal{L} = 1400\eta$, and (a3),(b3),(c3) $0.44\mathcal{L} = 310\eta$. The results of S2048 ($R_\lambda = 740$).

in Ref. [45], it is wrong and the theory cannot describe the clusters with St $\gg 1$ [41]. Here, we propose a much simpler generalization to describe the clusters with an arbitrary St in the range $1 \lesssim \mathrm{St} \lesssim \mathcal{T}/\tau_\eta$. We also verify the assumptions and results of the generalized mechanism (the generalized SSM, GSSM) by using DNS of developed turbulence in a periodic cube.

II. DIRECT NUMERICAL SIMULATIONS

A. Governing equations

We investigate the motion of small heavy spherical solid particles in turbulent flow of an incompressible fluid. The velocity $\boldsymbol{u}(\boldsymbol{x}, t)$ and pressure $p(\boldsymbol{x}, t)$ of the fluid at the position $\boldsymbol{x}$ and

TABLE I. Parameters and statistics of the simulated turbulence: N^3, the number of Fourier modes; $\boldsymbol{f}$, external force; R_λ, Taylor-length Reynolds number; $\mathcal{L}$, integral length; η, Kolmogorov length; $\mathcal{T}$, integral time; τ_η, Kolmogorov time; $k_{\max}$ $(=\sqrt{2}N/3)$, the largest resolved wave number. The statistical values are temporal averages over the period of $15\mathcal{T}$ for S2048, $100\mathcal{T}$ for S0512, and $30\mathcal{T}$ for R0512.

Case	N^3	$\boldsymbol{f}$	R_λ	$\mathcal{L}$	η	$\mathcal{L}/\eta$	$\mathcal{T}/\tau_\eta$	$k_{\max}\eta$
S2048	2048^3	$\boldsymbol{f}^{(S)}$	740	1.1	1.4×10^{-3}	800	58	1.4
S0512	512^3	$\boldsymbol{f}^{(S)}$	290	1.1	5.2×10^{-3}	220	25	1.3
R0512	512^3	$\boldsymbol{f}^{(R)}$	250	1.2	5.4×10^{-3}	230	28	1.3

time t are governed by the Navier-Stokes equation,

$$\frac{\partial \boldsymbol{u}}{\partial t} + \boldsymbol{u}\cdot\nabla\boldsymbol{u} = -\frac{1}{\rho_f}\nabla p + \nu\nabla^2\boldsymbol{u} + \boldsymbol{f}, \tag{2}$$

with an external force $\boldsymbol{f}$ and the equation of continuity,

$$\nabla\cdot\boldsymbol{u} = 0. \tag{3}$$

Here, ρ_f and ν denote the mass density and kinematic viscosity of the fluid, respectively. In (2), we assume that particles are small and dilute so that their effects on the fluid motion are negligible.

We also assume that each particle is subjected to the linear Stokes drag in fluid and their motion is governed by

$$\frac{d\boldsymbol{v}_p}{dt} = -\frac{1}{\tau_p}\{\boldsymbol{v}_p(t) - \boldsymbol{u}[\boldsymbol{x}_p(t), t]\}, \tag{4}$$

where $\boldsymbol{x}_p(t)$ and $\boldsymbol{v}_p(t)$ are the position and velocity of a particle at time t. In (4), τ_p $[=2\rho_p a^2/(9\rho_f\nu)]$ is the relaxation time of particle velocity, where a and ρ_p are the radius and mass density of a particle. Equation (4) holds under the following assumptions: (i) ρ_p is much larger than ρ_f; (ii) a is much smaller than the Kolmogorov length η $(=\epsilon^{-1/4}\nu^{3/4})$ of turbulence; (iii) the Reynolds number $\mathrm{Re}_p = |\boldsymbol{v}_p - \boldsymbol{u}|a/\nu$, based on a and the relative velocity between the particle and fluid, is sufficiently small; (iv) the gravity is neglected; and (v) there is no interaction between particles.

B. Numerical methods

The fluid motion is simulated by numerically integrating (2) and (3) by the fourth-order Runge-Kutta-Gill scheme under periodic boundary conditions (with the period being 2π) in three orthogonal directions. We evaluate the spatial derivatives by the Fourier spectral method, where the number of Fourier modes is $N^3 = 2048^3$ (in the case S2048; see Table I) and 512^3 (S0512 and R0512). We remove aliasing errors by the phase shift method. We conduct DNS with two different external forces: one is a steady force expressed by

$$\boldsymbol{f}^{(S)} = (-\sin x\cos y, +\cos x\sin y, 0), \tag{5}$$

and the other is a random force $\boldsymbol{f}^{(R)}$ [52]. We mainly use the DNS with $\boldsymbol{f}^{(S)}$, while the DNS with $\boldsymbol{f}^{(R)}$ is used for the verification (in Sec. IV C) of the assumptions of the proposed mechanism. In the following, k_f $(=\sqrt{2})$ denotes the magnitude of the wave-number vector of the Fourier transform of $\boldsymbol{f}^{(S)}$. We list the numerical parameters and statistics of the simulated turbulence in Table I. Since the indicator, $k_{\max}\eta$, of the resolution of the smallest-scale flow structures is about 1.5, they are not perfectly resolved. However, this is sufficient for the investigation of the inertial-range structures, which are the main target of the present study.

We track the inertial particles, whose initial positions are set homogeneous in space, by numerically integrating (4) by the fourth-order Runge-Kutta-Gill scheme. We evaluate the right-hand side of (4) by linearly interpolating the fluid velocity on the grid points. We investigate the cases with the Stokes number St defined by (1) being 0.63, 1.3, 2.5, 5.0, 10, 20, and 40 for S2048, and 0.062, 0.13, 0.25, 0.50, 1.0, 2.0, 4.0, 8.0, and 16 for S0512. The number of tracked particles is 1024^3 (S2048) and 512^3 (S0512) for each St.

Figure 1 shows the spatial distribution of the inertial particles with three different values of St (=1.3, 5.0, and 40) in turbulence at $R_\lambda = 740$. It is clear that the cluster size is larger for larger St. In Appendix A, we summarize the observations in Fig. 1, where we also show that the centrifugal mechanism [39,41] of coarse-grained coherent vortices of various sizes can explain the multiple-scale clusters. However, since such an explanation is qualitative, we develop in the next section an objective identification method of the clusters.

III. GENERALIZATION OF THE SWEEP-STICK MECHANISM

A. Sweep-stick mechanism

For the sake of completeness, we first briefly summarize the SSM [45], which we generalize in the next section. The SSM describes particle clusters by the surface $\mathcal{A}$ defined by

$$\boldsymbol{e}^{(1)} \cdot \boldsymbol{a} = 0 \qquad \text{and} \qquad \lambda^{(1)} > 0, \tag{6}$$

where $\boldsymbol{a}(\boldsymbol{x}, t)$ $(= \partial \boldsymbol{u}/\partial t + \boldsymbol{u} \cdot \nabla \boldsymbol{u})$ is the fluid acceleration, and $\lambda^{(i)}$ $(\lambda^{(1)} \geqslant \lambda^{(2)} \geqslant \lambda^{(3)})$ and $\boldsymbol{e}^{(i)}$ denote the three real eigenvalues and corresponding eigenvectors of the symmetric part of the acceleration gradient tensor $\nabla \boldsymbol{a}$. In the following, we explain the reason why $\mathcal{A}$ and particle clusters coincide. First, (4) leads to

$$\boldsymbol{v}_p - \boldsymbol{u}(\boldsymbol{x}_p, t) = -\tau_p \, \boldsymbol{a}(\boldsymbol{x}_p, t) + O(\tau_p^2). \tag{7}$$

Hence, if τ_p is sufficiently small (assumption C1),

$$\boldsymbol{v}_p - \boldsymbol{u}(\boldsymbol{x}_p, t) = -\tau_p \, \boldsymbol{a}(\boldsymbol{x}_p, t) \tag{8}$$

holds [21]. Let $\mathcal{A}^*$ be the surface on which $\boldsymbol{e}^{(1)} \cdot \boldsymbol{a} = 0$ is satisfied. Then, on $\mathcal{A}^*$,

$$\boldsymbol{e}^{(1)} \cdot \{\boldsymbol{v}_p - \boldsymbol{u}(\boldsymbol{x}_p, t)\} = 0 \tag{9}$$

holds by definition of $\mathcal{A}^*$. Since $\mathcal{A}^*$ is defined in terms of $\boldsymbol{a}$ and its gradient, which are predominantly determined by the smallest-scale coherent vortices, $\mathcal{A}^*$ also has coherence. It is therefore reasonable to assume (assumption C2) that $\mathcal{A}^*$ is advected in the local fluid velocity. Under the assumption (C2) and the assumption (assumption C3) that $\mathcal{A}^*$ and $\boldsymbol{e}^{(1)}$ are perpendicular, (9) implies that the relative velocity of a particle on $\mathcal{A}^*$ and the surface $\mathcal{A}^*$ is parallel to $\mathcal{A}^*$. Hence, particles on $\mathcal{A}^*$ move together with $\mathcal{A}^*$.

Under the assumption (C2), (8) implies that the compression rate of the relative distance between $\mathcal{A}^*$ and a particle is proportional to $\lambda^{(1)}\tau_p$. In other words, it takes about $1/(\lambda^{(1)}\tau_p)$ for a particle to accumulate on $\mathcal{A}^*$. Here, let T^{life} be the lifetime of $\mathcal{A}$, which is determined by the lifetime of the eddies of the Kolmogorov scale. Then, when

$$\tau_p > 1/(T^{\text{life}}\lambda^{(1)}) \qquad \text{(assumption C4)}, \tag{10}$$

the particle with τ_p can accumulate onto $\mathcal{A}^*$ along a path parallel to $\boldsymbol{e}^{(1)}$. Note that $\lambda^{(1)}$ must be positive, because of the minus sign on the right-hand side of (8), so that $\boldsymbol{e}^{(1)}$ is a compression direction. Hence, the subset of $\mathcal{A}^*$ with the condition $\lambda^{(1)} > 0$, i.e., (6), defines $\mathcal{A}$ which expresses particle clusters.

In summary, the SSM is valid under the four assumptions (C1)–(C4) (see Table II). Assumption (C2) was verified in Ref. [45], and the generalization of (C3) will be verified in Sec. IV C (Fig. 7). Note that the characteristics of turbulence, rather than of the particles, are relevant to these assumptions. Hence, assumptions (C1) and (C4) limit the range of τ_p for the mechanism to be valid.

TABLE II. Assumptions of the SSM and GSSM.

SSM	
C1	$\boldsymbol{v}_p - \boldsymbol{u} = -\tau_p \boldsymbol{a}$ (8)
C2	$\mathcal{A}$ is advected by the local velocity $\boldsymbol{u}$.
C3	$\mathcal{A} \perp \boldsymbol{e}^{(1)}$
C4	$\tau_p > 1/(T^{\rm life}\lambda^{(1)})$ (10)
GSSM	
G1	If particles with a given τ_p form clusters ($> \ell$), they also form the clusters in $\boldsymbol{u}_c(\boldsymbol{x}, t; \ell)$. $\boldsymbol{v}_c - \boldsymbol{u}_c = -\tau_p \boldsymbol{a}_c$ (14)
G2	$\mathcal{A}_c$ is advected by the local velocity $\boldsymbol{u}_c$.
G3	$\mathcal{A}_c \perp \boldsymbol{e}_c^{(1)}$
G4	$\tau_p > 1/\left(T_c^{\rm life}\lambda_c^{(1)}\right)$ (16)

First, we consider the requirement for (C4). We estimate by the present and lower-R_λ DNS that the average $\langle\lambda^{(1)}\rangle$ is $0.42\tau_\eta^{-2}$ (at $R_\lambda = 81$), $0.45\tau_\eta^{-2}$ (290), and $0.49\tau_\eta^{-2}$ (740); namely, it satisfies $\lambda^{(1)} \sim \tau_\eta^{-2}$, although it is a weakly increasing function of R_λ due to the spatial intermittency. Thus, (10) can be rewritten as $\tau_p > \tau_\eta^2/T^{\rm life}$. Since the lifetime $T^{\rm life}$ of Kolmogorov-scale vortices is comparable with (or longer than) τ_η, (10) is approximated by $\tau_p > c_4\tau_\eta$, where $c_4 (\lesssim 1)$ is a constant. Assumption (C1), on the other hand, holds when $\tau_p < \tau_\eta$ [21]. Hence, in order to satisfy (C1) and (C4) simultaneously, it is necessary that $\tau_p \approx \tau_\eta$ (i.e., St ≈ 1). In fact, Fig. 1 of Ref. [45] shows the cluster of particles with St $= 2$ coincides with $\mathcal{A}$. However, assumption (C1) does not hold for St $\gg 1$. Therefore, the SSM cannot describe clusters of particles with St $\gg 1$. In the next section, we develop a generalization which can apply to the cases with St $\gg 1$.

B. Generalized sweep-stick mechanism

As discussed above, the reason why the SSM cannot describe the clusters of particles with St $\gg 1$ is that (C1) is invalid for St $\gg 1$. However, as will be shown below, the extension of the SSM for St $\gg 1$ is straightforward.

For preparation, we introduce the coarse-grained fluid velocity $\boldsymbol{u}_c(\boldsymbol{x}, t; \ell)$ and acceleration $\boldsymbol{a}_c(\boldsymbol{x}, t; \ell)$ at the length scale ℓ. We estimate $\boldsymbol{u}_c$ by a low-pass filter of the Fourier modes with the sharp cut-off wave number $k_c = 2\pi/\ell$ and $\boldsymbol{a}_c$ by

$$\boldsymbol{a}_c = -(\nabla p_c)/\rho_f + \nu\nabla^2\boldsymbol{u}_c + \boldsymbol{f}_c, \tag{11}$$

where p_c is the solution to the Poisson equation,

$$\nabla^2 p_c = -\rho_f \nabla \cdot [\boldsymbol{u}_c \cdot \nabla \boldsymbol{u}_c], \tag{12}$$

and $\boldsymbol{f}_c$ is the coarse-grained external force. Here, we define $\boldsymbol{a}_c$ by (11) instead of the direct coarse-graining of $\boldsymbol{a}$, since the pressure gradient plays an essential role in the dynamics in the inertial range, and since the coarse-grained pressure p_c defined by (12) captures the inertial-scale coherent structures (see Fig. 6 of Ref. [42]).

We can generalize the SSM by using $\boldsymbol{u}_c$ and $\boldsymbol{a}_c$. If particles with a given τ_p form clusters by the action of vortices of size ℓ, they also form similar clusters in the imaginary velocity field $\boldsymbol{u}_c$ coarse-grained at ℓ. More precisely, let us suppose the particles whose velocity $\boldsymbol{v}_c (= d\boldsymbol{x}_c/dt)$ is governed by

$$\frac{d\boldsymbol{v}_c}{dt} = -\frac{1}{\tau_p}\{\boldsymbol{v}_c(t) - \boldsymbol{u}_c[\boldsymbol{x}_c(t), t]\}, \tag{13}$$

instead of (4). Then, such imaginary particles also form the same clusters of size ℓ as the real particles (assumption G1). Similarly to assumption (C1), we can estimate the relative velocity by

$$\boldsymbol{v}_c - \boldsymbol{u}_c(\boldsymbol{x}_c, t; \ell) = -\tau_p \, \boldsymbol{a}_c(\boldsymbol{x}_c, t; \ell). \tag{14}$$

We expect that (14), which is derived from (13), is valid when τ_p is sufficiently smaller than $T(\ell)$. Here, $T(\ell)$ denotes the turnover time of eddies of size ℓ. See Ref. [53] for an additional explanation.

Then, in a similar manner to obtain (6) of the SSM, we can show that the spatial distribution of the clusters of inertial particles is described by the surface $\mathcal{A}_c$ expressed by

$$\boldsymbol{e}_c^{(1)} \cdot \boldsymbol{a}_c = 0 \qquad \text{and} \qquad \lambda_c^{(1)} > 0. \tag{15}$$

Here, $\lambda_c^{(1)} \geqslant \lambda_c^{(2)} \geqslant \lambda_c^{(3)}$ denote the eigenvalues of the symmetric part of $\boldsymbol{\nabla a}_c$ and $\boldsymbol{e}_c^{(i)}$ is the eigenvector corresponding to $\lambda_c^{(i)}$.

Since the GSSM is an extension of SSM, it holds under the four assumptions which are similar to the SSM assumptions (C1)–(C4) (see Table II). In addition to (G1) mentioned above, we require (G2) $\mathcal{A}_c$ is advected by the coarse-grained velocity $\boldsymbol{u}_c$; (G3) $\mathcal{A}_c$ is perpendicular to $\boldsymbol{e}_c^{(1)}$; and (G4) the time, $1/(\lambda_c^{(1)}\tau_p)$, taken for a particle to accumulate on $\mathcal{A}_c$ is smaller than the lifetime of $\mathcal{A}_c$. Similarly to (C4), (G4) is expressed by

$$\tau_p > 1/\left(T_c^{\text{life}} \lambda_c^{(1)}\right), \tag{16}$$

where T_c^{life} denotes the lifetime of $\mathcal{A}_c$. Therefore, assuming that $T_c^{\text{life}}(\ell) \gtrsim T(\ell)$ and $\lambda_c^{(1)} \sim T(\ell)^{-2}$ (see Fig. 8 below), (G4) requires $\tau_p > c_4 T(\ell)$ with a constant c_4 (<1). Incidentally, the above arguments predict that particles form clusters around $\mathcal{A}_c$ with a finite thickness $r \sim \ell \exp\left[-T_c^{\text{life}}(\ell)\tau_p/T(\ell)^2\right]$ because the contraction rate of particles onto $\mathcal{A}_c$ is $\lambda_c^{(1)}\tau_p \sim \tau_p/T(\ell)^2$.

Hence, in order that (G1) and (G4) simultaneously hold, we need to choose the coarse-graining scale ℓ (or the cut-off wave number $k_c = 2\pi/\ell$) such that $\tau_p \approx T(\ell)$. Since, according to the Kolmogorov similarity, $T(\ell) \sim \epsilon^{-1/3}\ell^{2/3}$, the validity condition of the GSSM is expressed by

$$\tau_p \sim \epsilon^{-1/3}\ell^{2/3}, \tag{17}$$

or equivalently, in terms of St ($=\tau_p/\tau_\eta$),

$$\text{St} \sim (\ell/\eta)^{2/3}. \tag{18}$$

We will verify (18) in Sec. IV B.

IV. NUMERICAL VERIFICATION OF THE MECHANISM

In this section, we numerically verify the GSSM. First, in Sec. IV A, we show the relationship between $\mathcal{A}_c$ defined by (15) and coherent vortices in turbulence. Then, in Sec. IV B, we show the direct evidence that the clusters of inertial particles are well expressed by $\mathcal{A}_c$ with the appropriately chosen coarse-graining scale ℓ according to (17). Finally, in Sec. IV C, we show the numerical verification of the four assumptions of the GSSM, which are summarized in Table II.

A. Identification of surfaces $\mathcal{A}_c$

We identify $\mathcal{A}_c$ by the procedure described in Appendix B. Figure 2 shows examples of $\mathcal{A}_c$ for three different values of k_c in turbulence at $R_\lambda = 740$ (run S2048). The most important observation in Fig. 2 is that $\mathcal{A}_c$ is composed of coherent surfaces and their characteristic length is larger for smaller k_c (larger ℓ).

Here, we show that $\mathcal{A}_c$ reflects coherent vortices at scale $\ell = 2\pi/k_c$. Recall that this high-R_λ turbulence is composed of the hierarchy of coherent tubular vortices (see Fig. 9 in Appendix A). First, let us look at Fig. 2(a) for $k_c = \sqrt{2}k_f$. The surfaces $\mathcal{A}_c$ shown in Fig. 2(a) are located at $x = 0, \pi$ and $y = 0, \pi$, which are the location of $\mathcal{A}$ [defined by (6) without the coarse-graining of

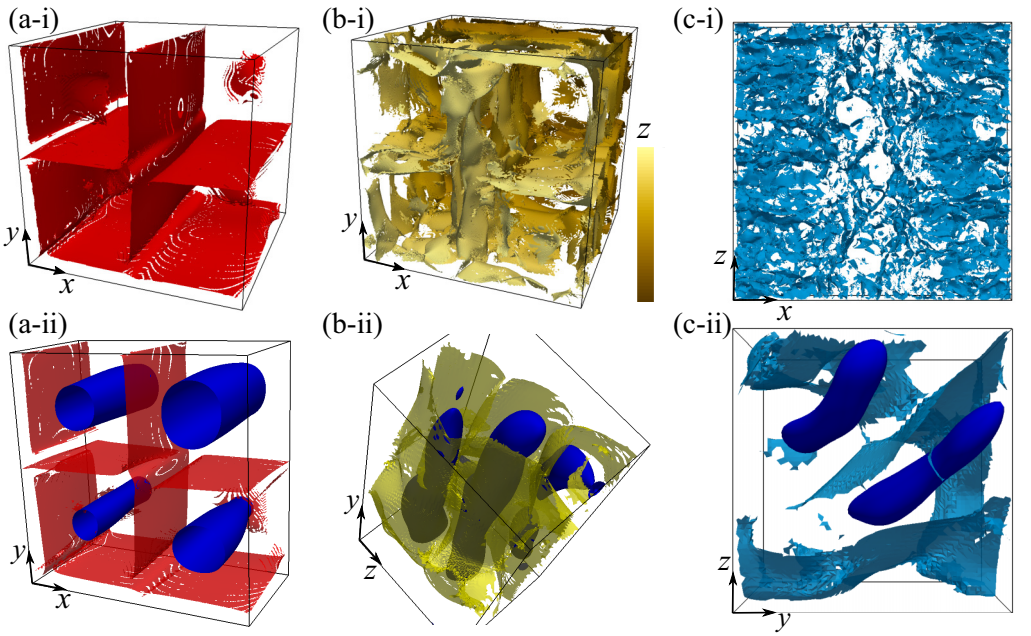

FIG. 2. (a-i), (b-i), (c-i) The surfaces $\mathcal{A}_c(k_c)$ defined by (15) in turbulence (S2048) for the cut-off wave number: (a-i) $k_c = \sqrt{2}k_f$ ($\ell = 2200\eta$), (b-i) $4\sqrt{2}k_f$ (550η), and (c-i) $16\sqrt{2}k_f$ (140η). In (b-i), the color indicates the z coordinate. (a-ii), (b-ii), (c-ii) $\mathcal{A}_c(k_c)$ together with the isosurface (dark-blue objects) of the coarse-grained enstrophy $\mathcal{E}_c$ with the cut-off wave number k_c. Panels (b-ii) and (c-ii) are the magnification of (b-i) and (c-i), respectively. The threshold of $\mathcal{E}_c$ is taken as (a-ii) $\mu + 1.5\sigma$, (b-ii) $\mu + 1.2\sigma$, and (c-ii) $\mu + 3\sigma$. Here, μ and σ denote the spatial average and standard deviation of $\mathcal{E}_c$, respectively. The shown domain size is (a-i), (b-i) $(4500\eta)^3$, (c-i) $4500\eta \times 350\eta \times 4500\eta$, (a-ii) $4500\eta \times 4500\eta \times 2200\eta$, (b-ii) $1100\eta \times 2900\eta \times 1400\eta$, and (c-ii) $300\eta \times 450\eta \times 460\eta$.

a] of the steady flow,

$$\boldsymbol{u} = \frac{(-\sin x \cos y, \cos x \sin y, 0)}{2\nu}. \tag{19}$$

The steady flow (19) is stably sustained by the balance between the body force (5) and viscous effects at low-Reynolds numbers. The similarity between $\mathcal{A}_c$ [Fig. 2(a-i)] in the high-Reynolds number turbulence and $\mathcal{A}$ in the steady flow (19) is consistent with the observation that the large-scale vortices sustained by the force (5) are always embedded in turbulence irrespective of the Reynolds number [42]. In fact, the isosurfaces of the coarse-grained enstrophy [Fig. 2(a-ii)] in the developed turbulence and those of the enstrophy (without the coarse-graining) in the steady flow (19) are also similar (figure is omitted). It is further important that $\mathcal{A}_c$ in Fig. 2(a-i) is located between those largest-scale vortex tubes.

We observe a similar relationship between $\mathcal{A}_c$ and coherent tubular vortices for larger k_c (i.e., smaller scales) too. Figures 2(b) and 2(c) show $\mathcal{A}_c$ for k_c 4 times and 16 times larger than k_c in Fig. 2(a), respectively. As demonstrated in Figs. 2(b-ii) and 2(c-ii), irrespective of k_c, $\mathcal{A}_c$ surrounds the vortices, which are visualized by the isosurfaces of the enstrophy coarse-grained with the cut-off wave number k_c. This fact gives the basis of assumption (G2), that is, $\mathcal{A}_c$ is coherent and advected by the local coarse-grained velocity.

Since the centrifugal mechanism [39] predicts the accumulation of particles in the low-vorticity high-strain regions of coarse-grained field, these observations in Figs. 2(a-ii), 2(b-ii), and 2(c-ii) are

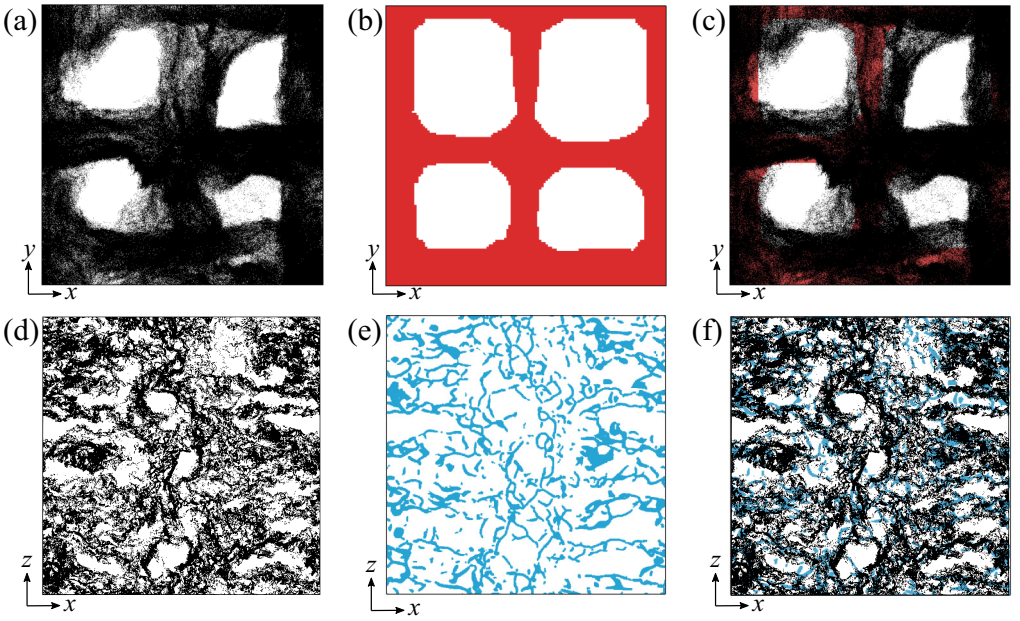

FIG. 3. (a), (d) Spatial distribution of inertial particles [(a) St = 40, (b) 5.0] in a thin layer (with thickness 10η). (b), (e) Cross section of $\mathcal{A}_c$ with the plane at the center of the thin layer for (b) $k_c = \sqrt{2}k_f$ and (e) $16\sqrt{2}k_f$. The width of $\mathcal{A}_c$ is set to be $\pi/(2k_c)$ [i.e., (b) 560η and (e) 35η]. (c), (f) Superposition of (a), (b) and (d), (e). Results of S2048.

consistent with our claim (Sec. III B) that $\mathcal{A}_c$ describes the particle clusters. In the next section, we will show this in more detail.

B. Spatial correlation between particles and $\mathcal{A}_c$

Figure 3 compares the spatial distributions of (a), (d) particles and (b), (e) $\mathcal{A}_c$. The Stokes number is (a), (c) St = 40 and (d), (f) 5.0. It is evident that $\mathcal{A}_c$ coincides with the clusters of the inertial particles with St $\gg 1$ [Figs. 3(c) and 3(f)] if we choose the cut-off wave number appropriately ($k_c = \sqrt{2}k_f$ for St = 40; $16\sqrt{2}k_f$ for St = 5.0) according to St. Note that we show $\mathcal{A}_c$ in Fig. 3 with a thickness r, which is chosen as follows. As discussed in Sec. III B, particles distribute around $\mathcal{A}_c$ with a thickness $r \sim \ell \exp[-T_c^{\rm life}(\ell)\tau_p/T(\ell)^2]$. We have chosen ℓ so that $T(\ell) \approx \tau_p$ and we may assume $T_c^{\rm life} \sim T(\ell)$, then the thickness r is estimated by $r \sim \ell \sim (k_c)^{-1}$. Therefore, we set $r = \pi/(2k_c)$ in Fig. 3, where we have empirically chosen the prefactor $(\pi/2)$. Although the coincidence of the particle clusters and $\mathcal{A}_c$ is good, it is not perfect. We will discuss the cause of the discrepancy in Sec. IV C.

Next, we consider the optimal k_c, which is denoted by k_c^*, for the particles with a given St. More concretely, we determine k_c^* by the cut-off wave number for which the spatial correlation between $\mathcal{A}_c$ and the particles becomes the maximum, and verify the scaling (18), or equivalently,

$$\mathrm{St} \sim (k_c^*\eta)^{-2/3}. \tag{20}$$

For this purpose, we introduce the functions $\chi_i^{\mathcal{A}}(k_c, t)$ and $\chi_i^P(\mathrm{St}, t)$ which characterize the spatial distributions of $\mathcal{A}_c$ and particles, respectively. We divide the entire computational domain into smaller cubes with side $r = \pi/(2k_c)$, and we define the function $\chi_i^{\mathcal{A}}$ (or χ_i^P) to be 1 if $\mathcal{A}_c$ (or a particle) exists in the ith cube; or to be 0 otherwise. Note that we set $r = \pi/(2k_c)$ as in Fig. 3. Then,

we evaluate the spatial correlation between $\mathcal{A}_c$ and the particles by

$$C(k_c, \mathrm{St}, r) = \frac{\left\langle\!\left\langle \left[\chi_i^{\mathcal{A}}(k_c,t) - \langle\!\langle \chi^{\mathcal{A}} \rangle\!\rangle(k_c)\right]\left[\chi_i^{P}(\mathrm{St},t) - \langle\!\langle \chi^{P} \rangle\!\rangle(\mathrm{St})\right] \right\rangle\!\right\rangle}{\sqrt{\left\langle\!\left\langle \left[\chi_i^{\mathcal{A}}(k_c,t) - \langle\!\langle \chi^{\mathcal{A}} \rangle\!\rangle(k_c)\right]^2 \right\rangle\!\right\rangle \left\langle\!\left\langle \left[\chi_i^{P}(\mathrm{St},t) - \langle\!\langle \chi^{P} \rangle\!\rangle(\mathrm{St})\right]^2 \right\rangle\!\right\rangle}}. \tag{21}$$

Here, $\langle\!\langle \cdot \rangle\!\rangle$ denotes the spatio-temporal average. We show in Fig. 4 the correlation C as a function of k_c for two different Reynolds numbers: (a) $R_\lambda = 290$ (run S0512) and (b) 740 (S2048). For each St and R_λ, we can determine k_c^* as the wave number which maximizes C.

Looking at the curves with symbols ($\triangledown$, $\blacktriangledown$, $\circ$, $\bullet$, and $\triangle$) in Fig. 4(a) for $\mathrm{St} \leqslant 1$, we notice that the maximum value of C for $\mathrm{St} \lesssim 1$ is larger for larger St, and k_c^* is constant to be about $0.3/\eta$ [see also Fig. 4(c)]. This is reasonable because the Kolmogorov-scale vortices predominantly contribute to the clustering of particles with $\mathrm{St} \lesssim 1$ and because the clusters form faster for larger τ_p. We plot the optimal wave number k_c^* in Fig. 4(c) as a function of St. We can see that k_c^* is a decreasing function of St for $1 \lesssim \mathrm{St} \lesssim 10$ in both cases of R_λ. More importantly, in the higher Reynolds number ($R_\lambda = 740$, run S2048) case, we observe that (20) holds in the St range $1 \lesssim \mathrm{St} \lesssim 10$.

In contrast, for $R_\lambda = 290$ (run S0512), the scaling (20) is unclear. We can explain this as follows. Looking again at Figs. 4(a) and 4(b), we notice that C is rather broad for a given St. More precisely, C takes non-negligible values for $k_c^*/10 \lesssim k_c \lesssim 10k_c^*$. This implies that the particles are affected by the vortices in a wide [say, $O(100)$] range of length scales, which corresponds to the time-scale range of the ratio about 22 ($=100^{2/3}$). Hence, since the time-scale ratio is $\tau_\eta/\mathcal{T} = 25$ for S0512 (see Table I), the scaling (20) cannot be clear. We will also discuss, in the next section, this multiple-scale nature of the particle clusters.

For further larger St (namely, $\mathrm{St} \geqslant 8$ for S0512 and $\mathrm{St} \geqslant 10$ for S2048), k_c^* is a constant about $0.083/\eta$ (S0512) or $0.023/\eta$ (S2048), both of which correspond to $18/\mathcal{L}$ (see Table I for the value of $\mathcal{L}/\eta$ in each case). This is reasonable because there are no vortices, and therefore no $\mathcal{A}_c$, larger than $\mathcal{L}$. For the same reason, the maximum value of C is smaller for larger St [Figs. 4(a) and 4(b)].

Incidentally, Fig. 4(c) suggests that the scaling (20) holds in the range of St:

$$1 < \mathrm{St} < 0.08\left(\frac{\mathcal{L}}{\eta}\right)^{2/3} \approx 0.01 R_\lambda, \tag{22}$$

the upper bound of which is estimated by the results of S2048 and the scaling $R_\lambda \sim (\mathcal{L}/\eta)^{2/3}$. Equation (22) explains again why (20) is unclear for S0512 ($R_\lambda = 290$).

C. Verification of the assumptions

Before closing the present article, we numerically verify each of the assumptions of the GSSM (Table II).

1. Assumption (G1)

First, we verify the assumption (G1). For this purpose, we track particles, according to (13), in coarse-grained fields $\boldsymbol{u}_c$ [54]. Figures 5(a)–5(d) show the spatial distribution of such imaginary particles with $\mathrm{St} = 4$ in $\boldsymbol{u}_c(\boldsymbol{x}, t; \ell)$ and 5(e)–5(h) $\mathcal{A}_c(\ell)$ in the coarse-grained fields, where the coarse-graining scale ℓ is set as (a), (e) $\ell = 50\eta$, (b), (f) 100η, (c), (g) 250η, and (d), (h) 500η. Note that the particle distribution shown in Fig. 5(a) with the small ℓ ($=50\eta$) is almost the same as the spatial distribution of particles in $\boldsymbol{u}$ without coarse-graining (figure is omitted). Note also that the clusters have multiple length scales. Looking at Figs. 5(a)–5(d), we see that as ℓ increases the (minimum) length scale in the particle clusters gets larger, and particle clusters in Fig. 5(a) contain larger clusters in Figs. 5(b)–5(d). This is direct evidence of the assumption (G1); for example, since particles form clusters at the scale $\ell = 250\eta$ in the real field $\boldsymbol{u}$ [Fig. 5(a)], the imaginary particles in the coarse-grained field $\boldsymbol{u}_c(\boldsymbol{x}, t; \ell = 250\eta)$ also form similar clusters of size $\ell = 250\eta$ [Fig. 5(c)].

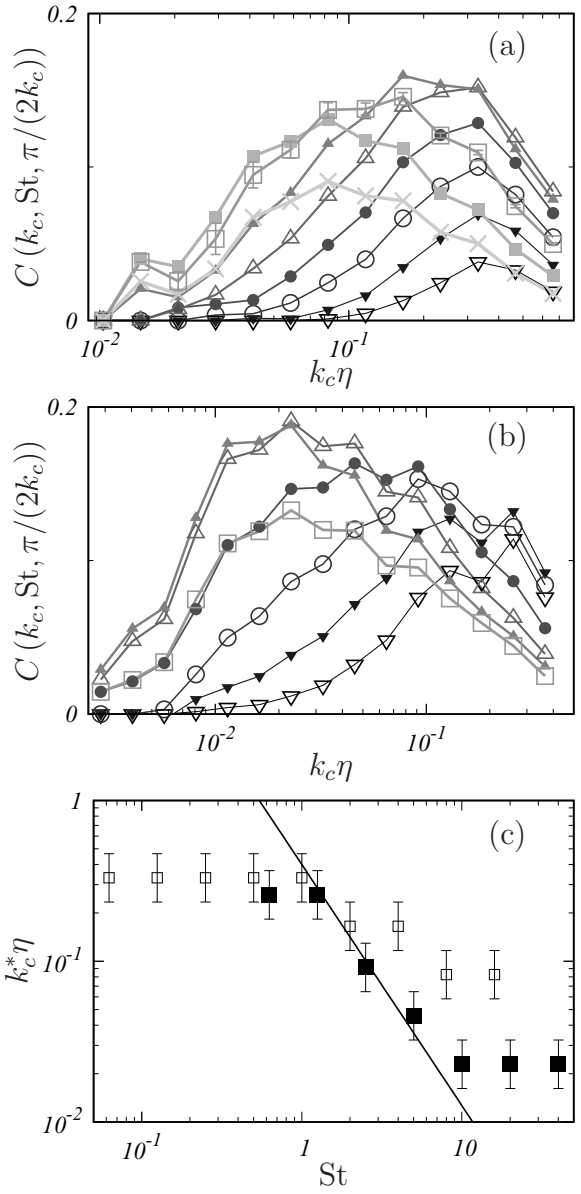

FIG. 4. Spatial correlation C between $\mathcal{A}_c$ and particles as a function of k_c for (a) $R_\lambda = 290$ and (b) 740. Different curves are for different St: (a) ▽, St = 0.062; ▼, 0.13; ○, 0.25; ●, 0.50; △, 1.0; ▲, 2.0; □, 4.0; ■, 8.0; ×, 16. (b) ▽, St = 0.63; ▼, 1.3; ○, 2.5; ●, 5.0; △, 10; ▲, 20; □, 40. The error bars for St = 4 (□) in (a) show the standard deviation for different snapshots. (c) Optimal k_c^* as a function of St for $R_\lambda = 290$ (□) and 740 (■). The solid line indicates $k_c^*\eta = 0.4\,\mathrm{St}^{-3/2}$.

Here, we discuss the cause of the imperfect coincidence (Fig. 3) of particle clusters of a given St and $\mathcal{A}_c(\ell)$. Looking at Figs. 5(a) and 5(e), we see that some parts of small-scale $\mathcal{A}_c$ in Fig. 5(e) well coincide with the particle clusters in Fig. 5(a), but there are no particles around other parts of $\mathcal{A}_c$. (Recall that the particle clusters shown in Fig. 5(a) are almost identical to the particle distribution in the real field $\boldsymbol{u}$ without the coarse-graining.) More accurately, $\mathcal{A}_c$ in Fig. 5(e) surrounded by

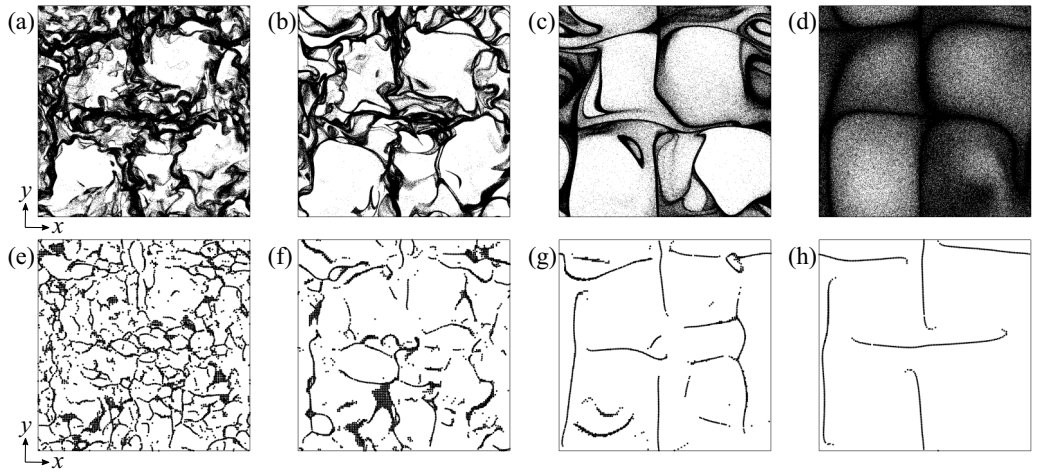

FIG. 5. (a)–(d) Clustering of particles with $\mathrm{St} = 4$ in the coarse-grained field $\boldsymbol{u}_c(\boldsymbol{x}, t; \ell)$ in a thin layer ($1200\eta \times 1200\eta \times 10\eta$) perpendicular to the z axis. (e)–(h) $\mathcal{A}_c$ in the same layer. Result of S0512. The coarse-graining scale is set as (a), (e) $\ell = 50\eta$, (b), (f) 100η, (c), (g) 250η, and (d), (h) 500η.

larger $\mathcal{A}_c$ shown in Figs. 5(f) and 5(g) do not attract the particles. This is reasonable. Since the clustering condition holds for broad length scales ℓ, larger eddies slowly centrifuge out particles to form larger void regions. Once such a void is formed, $\mathcal{A}_c$ in the void for smaller scales cannot attract particles because there are no particles around them. Therefore, the particle clusters [e.g., Fig. 5(a)] which generally depend on initial particle distributions, may be described by a selective superposition of $\mathcal{A}_c$ observed in Figs. 5(e)–5(g). These observations also explain the reason why the correlation coefficient C (Fig. 4) takes relatively small values in a rather broad range of k around k_c^*.

2. Assumption (G2)

Next, we verify the assumption (G2). Figure 6(a) shows points on the surfaces $\mathcal{A}_c$ for $k_c = 16\sqrt{2}k_f$ at time t (blue) and $t + T(\ell)$ (red). Here, we estimate $T(\ell)$ by $\langle \mathcal{E}_c(\ell) \rangle^{-1/2}$ ($\mathcal{E}_c$ is the coarse-grained enstrophy). We can see that $\mathcal{A}_c$ moves with keeping its coherence. The gray points in Fig. 6(b) are obtained by the advection of the blue points in Fig. 6(a) with the local coarse-grained velocity $\boldsymbol{u}_c$. The time increment of the advection is set to be $T(\ell)$. The surfaces expressed by the set of these gray points are in good agreement with $\mathcal{A}_c$ at $t + T(\ell)$ (red points); the correlation coefficient, which is evaluated by a similar method to (21), between these two sets is about 0.6. This supports the assumption (G2). Incidentally, (G2) does not hold for $k_c \approx k_f$ (figure is omitted). This is because $\mathcal{A}_c$ reflects the coherent vortical structures at scale $\ell = 2\pi/k_c$ (see Sec. IV A), and because the vortices, and therefore $\mathcal{A}_c$, for $\ell \ll \mathcal{L}$ are swept by the flow induced by vortices larger than ℓ. When $\ell \approx \mathcal{L}$, however, this picture does not hold because the scale separation is insufficient. In conclusion, (G2) holds for $\ell \lesssim \mathcal{L}$.

3. Assumption (G3)

Figure 7 shows the probability density function of the cosine of the angle θ between the normal vector $\boldsymbol{n}$ of $\mathcal{A}_c$ and the eigenvector $\boldsymbol{e}_c^{(1)}$ of the symmetric part of $\nabla \boldsymbol{a}_c$. More precisely, $\boldsymbol{n}$ is the normal vector of a triangle which composes $\mathcal{A}_c$, and $\boldsymbol{e}_c^{(1)}$ is evaluated at the center of the triangle. In Fig. 7, we show the results for three values of k_c for each turbulence driven by the two different forcings. In all the cases, irrespective of the forcing, we can see the strong tendency $\boldsymbol{n} \parallel \boldsymbol{e}_c^{(1)}$ (i.e., $\mathcal{A}_c \perp \boldsymbol{e}_c^{(1)}$). Note that the isotropic angle distribution leads to $P(|\cos\theta|) = 1$. Therefore, Fig. 7 gives the direct

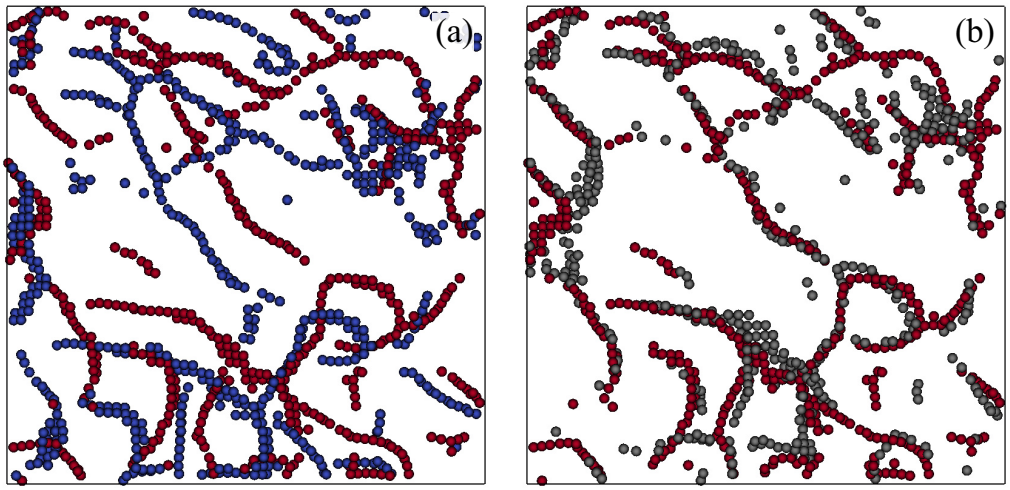

FIG. 6. (a) Spatial distribution of points on the surfaces $\mathcal{A}_c$ (for $k_c = 16\sqrt{2}k_f$) at time t (blue points) and $t + T(\ell)$ (red points) on a cross section of size $(260\eta)^2$. (b) $\mathcal{A}_c$ at $t + T(\ell)$ (red) and the points (gray) which are on $\mathcal{A}_c$ at t and advected, for the duration $T(\ell)$, by local $\boldsymbol{u}_c$. Results of S0512.

verification of assumption (G3). It is also interesting to observe that the angle distribution seems to be universal independent of the forcing scheme and k_c, if k_c is sufficiently large. Incidentally, the gray dashed line in Fig. 7(a) deviates from the universal curve. This stems from the fact that $\mathcal{A}_c$ for the largest scale [Fig. 2(a-i)] in the turbulence driven by the steady force (5) resembles $\mathcal{A}$ in the steady flow (19), for which $\mathcal{A} \perp \boldsymbol{e}^{(1)}$ strictly holds at any point on $\mathcal{A}$.

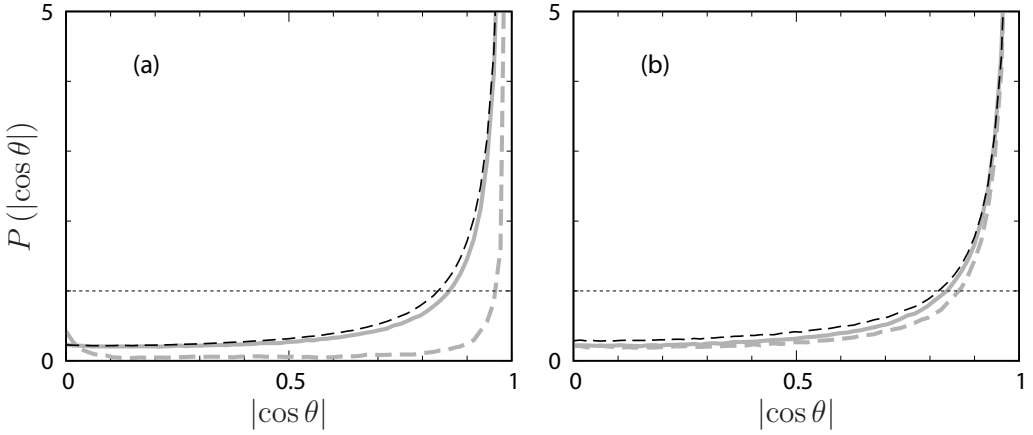

FIG. 7. Probability density function of $|\cos\theta|$ of the angle θ between the normal vector $\boldsymbol{n}$ of $\mathcal{A}_c$ and the eigenvector $\boldsymbol{e}_c^{(1)}$. Results of (a) S0512 and (b) R0512. (a) Gray dashed line, $k_c = \sqrt{2}k_f$ $(=0.010\eta^{-1})$; gray solid line, $4\sqrt{2}k_f$ $(=0.041\eta^{-1})$; black dashed line, $16\sqrt{2}k_f$ $(=0.17\eta^{-1})$. (b) Gray dashed line, $k_c = 0.022\eta^{-1}$; gray solid line, $0.087\eta^{-1}$; black dashed line, $0.35\eta^{-1}$. The horizontal dashed line, $P(|\cos\theta|) = 1$, indicates the isotropic distribution.

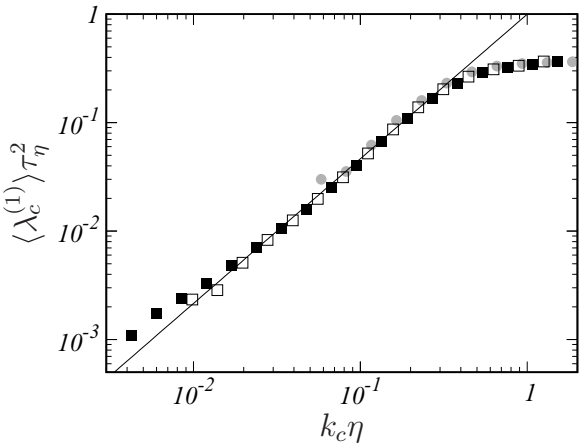

FIG. 8. Spatial average of $\lambda_c^{(1)}$ as a function of the cut-off wave number k_c for three different Reynolds numbers: •, $R_\lambda = 81$; □, 290 (S0512); ■, 740 (S2048). The solid line indicates $\langle \lambda_c^{(1)} \rangle = \epsilon^{2/3} k_c^{4/3}$.

4. Assumption (G4)

Concerning the assumption (G4), we have derived in Sec. III B the condition $\tau_p > c_4 T(\ell)$ under the further two assumptions (i) $T_c^{\rm life} \gtrsim T(\ell)$ and (ii) $\lambda_c^{(1)} \sim T(\ell)^{-2}$. Here, we verify the nontrivial assumption (ii), while (i) seems valid from observations (e.g., Fig. 6). Since $\ell = 2\pi/k_c$, (ii) is expressed by $\lambda_c^{(1)} \sim \epsilon^{2/3} k_c^{4/3}$, which is nondimensionalized by τ_η [$= (\nu/\epsilon)^{1/2}$] and η ($= \epsilon^{-1/4}\nu^{3/4}$) as

$$\lambda_c^{(1)} {\tau_\eta}^2 \sim (k_c\eta)^{4/3}. \tag{23}$$

We verify (23) in Fig. 8. The plots for the three different R_λ follow a single curve to indicate the universality of the statistics of $\lambda_c^{(1)}$. We can see that the scaling, $\lambda_c^{(1)} \sim k_c^{4/3}$, holds in the inertial range. In fact, the scaling range expands as R_λ increases. Hence, we conclude that (23) is valid if we consider the cut-off wave number k_c within the inertial range. In such a case, (G4) holds, when $\tau_p > c_4 T(\ell)$ with a constant c_4 (< 1).

V. CONCLUDING REMARKS

In the present study, we have examined the clustering of inertial particles due to the action of coherent structures in the inertial length and time scales in developed turbulence. The fluid acceleration plays an essential role in the examined clustering process. The SSM [45] defines, without a fitting parameter, the stagnation surface $\mathcal{A}$ by (6) which describes the particle clusters. However, the SSM is applicable only to the cases St ≈ 1 [41]. In the present article, we propose a GSSM (Sec. III B) to describe the particle clusters with any St in the range $1 \lesssim {\rm St} \lesssim \mathcal{T}/\tau_\eta$. In terms of the acceleration field coarse-grained at an appropriately chosen scale ℓ (or the cut-off wave number $k_c = 2\pi/\ell$), we can objectively define the surface $\mathcal{A}_c$ by (15) around which the particles accumulate (Fig. 3). The GSSM gives a first step to objectively describe particle clusters in turbulent flows, which is much more difficult than the examination of the clustering condition. However, looking at Fig. 4, we notice that the clusters are multiple-scale structures, for which rather board length scales ($2\pi/k_c$) contribute. This is consistent with the previous studies [25,29–31,39] that the clusters are fractal. Therefore, as discussed in Sec. IV C 1 in detail, we must consider the contributions from different length scales to accurately describe the fractal structures. More concretely, a selective superposition of $\mathcal{A}_c$ for different ℓ may be required to achieve this. We also reemphasize that the GSSM cannot apply to particle clusters caused by other mechanisms [26–28].

The GSSM holds under the four assumptions (G1)–(G4), which are summarized in Table II. We have verified them in Sec. IV C. The assumption (G1), which is an extension of the classical formula by Maxey [21], holds when $\tau_p \ll T(\ell)$. On the other hand, for the particles to accumulate onto $\mathcal{A}_c$ within the lifetime of $\mathcal{A}_c$, it is required that $\tau_p > c_4 T(\ell)$ ($c_4 < 1$); assumption (G4). Therefore, when we choose the coarse-graining scale ℓ such that $\tau_p \approx T(\ell)$, namely, (20), $\mathcal{A}_c$ can describe particle clusters. The DNS of high-Reynolds number turbulence ($R_\lambda = 740$) verifies the predicted scaling (20) [see Fig. 4(c)] of the optimal k_c. The visualization in Fig. 3 also supports the prediction. Once we choose k_c according to (20), the GSSM is a parameter-free theory which objectively describes particle clusters by $\mathcal{A}_c$. We also emphasize that the procedure (Appendix B) is simple and does not require an iterative method to find the stagnation surface $\mathcal{A}_c$ of $\boldsymbol{a}_c$.

As we have observed in Fig. 2, the surfaces $\mathcal{A}_c$ are located between tubular vortices at the coarse-graining scale ℓ. Therefore, the GSSM is consistent with the (generalized) centrifugal mechanism [39] that particles are swept out from the high-vorticity regions in the velocity field coarse-grained at ℓ. In other words, for the inertial-range clustering in high-Reynolds number turbulence, it is essential to make coarse-graining of the velocity field before the application of the classical centrifugal mechanism [21]. As pointed out in Ref. [41], this is also the case for the SSM; namely, we cannot apply the SSM to the inertial-range clustering. However, as demonstrated above, the generalization of the SSM is straightforward. We only have to coarse-grain the flow field before employing the SSM.

Here, note that particle clusters depend on the lifetime $T_c^{\rm life}$ of flow structures. We have reasonably assumed that $T_c^{\rm life} \approx T(\ell)$, but the lifetime of coherent vortices, in particular, large-scale eddies, depend on flow. For example, the steady vortices described by (19) induce the clustering of particles with τ_p much smaller than their turnover time $\mathcal{T}$ because of the infinite lifetime of the vortices. We emphasize that the present theory can also describe such an extreme case, since the assumption (G4) is expressed by (16) in terms of the lifetime of $\mathcal{A}_c$. It is an interesting future study to further develop the GSSM by taking into account the lifetime of $\mathcal{A}_c$ of each scale. Furthermore, since the GSSM does not rely on the statistical homogeneity or isotropy, we may apply it to inhomogeneous turbulence. This is also left for future studies.

ACKNOWLEDGMENTS

This study was partly supported by JSPS Grants-in-Aids for Scientific Research (Grants No. 16H04268 and No. 20H02068). The DNS were conducted under the support of the HPCI System Research Project (hp190116) and the NIFS Collaboration Research Programs (Grants No. NIFS18KNSS108 and No. NIFS20KNSS145).

APPENDIX A: SPATIAL DISTRIBUTION OF INERTIAL PARTICLES

Here, we briefly summarize observations in Fig. 1. (i) As is well known, the particle clusters are sharpest when $\mathrm{St} \approx 1$ [Fig. 1(a)]. The fine clusters observed in Fig. 1(a3) are explained by centrifugal effects [34] of the Kolmogorov-scale vortices. We show them in Fig. 9(c) in the same region as in Fig. 1(a3). The void regions of particles correspond to high-vorticity regions. Because of the hierarchy of vortices of various sizes (Fig. 9), particle clusters also exhibit a fractal-like structure [39].

(ii) Since R_λ ($=740$) is high enough, particles with $\mathrm{St} \gg 1$ also form clusters. For example, Fig. 1(c1) shows large-scale clusters of particles of $\mathrm{St} = 40$. This is also explained by the centrifugal effects. Since $\mathcal{T}/\tau_\eta = 58$ (Table I), $\mathrm{St} = 40$ corresponds to $\tau_p/\mathcal{T} = 0.69$. Therefore, the clusters in Fig. 1(c1) are formed by the effects of the largest vortices.

(iii) As St increases, smaller structures in the fractal-like clusters observed in (i) disappear. For example, looking at Fig. 1(b3) for $\mathrm{St} = 5.0$, which is four times larger than St in Fig. 1(a), we observe that the smallest-scale clusters observed in Fig. 1(a3) become obscure. Comparing Figs. 1(b2) and 1(c2), we can observe intermediate-scale voids in 1(b2) for $\mathrm{St} = 5.0$ but not in

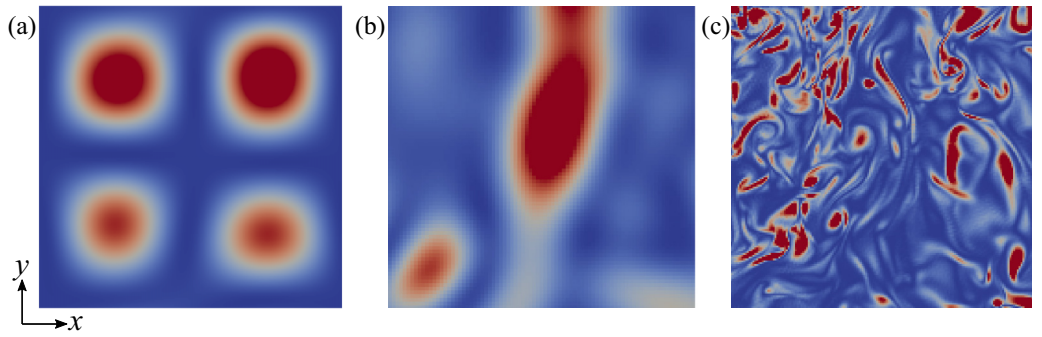

FIG. 9. Distribution of the coarse-grained enstrophy $\mathcal{E}_c$ on the plane at the center of the thin layer shown in Fig. 1. The color indicates the magnitude of $\mathcal{E}_c$ in the range between 0 (blue) and (a), (b) $\mu + 2\sigma$ and (c) μ (red), where μ and σ are the spatial average and standard deviation of $\mathcal{E}_c$, respectively. We evaluate the coarse-grained field by the low-pass filtering with a cut-off wave number k_c of the Fourier components of the velocity. The cut-off wave number is (a) $k_c = \sqrt{2}k_f$, (b) $4\sqrt{2}k_f$, and (c) ∞ (i.e., without the coarse-graining). The visualized region in (a), (b), and (c) is the same as that for Figs. 1(a1)–1(c1), 1(a2)–1(c2), and 1(a3)–1(c3), respectively. Results of S2048 ($R_\lambda = 740$).

1(c2) for St = 40. Since the particles cannot follow rapidly changing flow with time scales shorter than τ_p, they ignore the effects of such small-scale vortices.

(iv) Looking again at Fig. 1(a1) for St = 1.3, we observe particle voids at the same locations as in Fig. 1(c1). This observation is also important in the theory (Sec. III). Since the time scale $\mathcal{T}$ of the largest vortices is much longer than τ_p ($\tau_p/\mathcal{T} = 0.022 \ll 1$) for St = 1.3, the particles almost perfectly follow the fluid motion. However, the very weak centrifugal effect slowly sweeps the particles out. More quantitatively, we will show, in Sec. III B, that it takes about $T(\ell)^2/\tau_p$, where $T(\ell)$ is the turnover time of eddies of size ℓ, for the particles to be swept out. Hence, if the lifetime of the vortices is sufficiently longer than this, particle clusters are created by them. Recall that, in the present DNS, the largest vortices are long-lived because of the nature of the steady body force (5).

APPENDIX B: IDENTIFICATION PROCEDURE OF $\mathcal{A}_c$

In this Appendix, we describe the procedure to numerically identify the surface $\mathcal{A}_c$ defined by (15). In general, we need to employ an iterative method (e.g., the Newton method) to find points where (15) holds. However, since viscous effects and the external force are negligible for the coarse-grained acceleration $\boldsymbol{a}_c$, we can approximate $\boldsymbol{a}_c$ by $-(\nabla p_c)/\rho_f$. Then, the coarse-grained acceleration gradient tensor $\nabla \boldsymbol{a}_c$ is symmetric. In such case, since we can use a technique similar to the one developed in Refs. [55,56], it is rather straightforward to find $\mathcal{A}_c$.

First, we search the position $\boldsymbol{x} + \boldsymbol{\Delta}$ of a point, in the vicinity of each grid point $\boldsymbol{x}$, which satisfies $\boldsymbol{e}_c^{(1)} \cdot \boldsymbol{a}_c = 0$. When $|\boldsymbol{\Delta}|$ is small, $\boldsymbol{a}_c(\boldsymbol{x} + \boldsymbol{\Delta})$ is approximated by the Taylor series as

$$a_{ci}(\boldsymbol{x} + \boldsymbol{\Delta}) \approx a_{ci}(\boldsymbol{x}) + \left.\frac{\partial a_{ci}}{\partial x_j}\right|_{\boldsymbol{x}} \Delta_j, \tag{B1}$$

where a subscript i denotes the ith component of a vector. Because of the symmetry of $\nabla \boldsymbol{a}_c$, we obtain

$$\left.\frac{\partial a_{ci}}{\partial x_j}\right|_{\boldsymbol{x}} = \frac{1}{2}\left(\left.\frac{\partial a_{ci}}{\partial x_j}\right|_{\boldsymbol{x}} + \left.\frac{\partial a_{cj}}{\partial x_i}\right|_{\boldsymbol{x}} \right) = \sum_{m=1}^{3} \lambda_c^{(m)} e_{ci}^{(m)} e_{cj}^{(m)}. \tag{B2}$$

Then, we can rewrite (B1) as

$$\boldsymbol{a}_c(\boldsymbol{x}+\boldsymbol{\Delta}) = \boldsymbol{a}_c(\boldsymbol{x}) + \sum_{m=1}^{3} \lambda_c^{(m)} \left(\boldsymbol{\Delta}\cdot\boldsymbol{e}_c^{(m)}\right)\boldsymbol{e}_c^{(m)}. \tag{B3}$$

Here, we impose

$$\boldsymbol{a}_c(\boldsymbol{x}+\boldsymbol{\Delta})\cdot\boldsymbol{e}_c^{(1)}(\boldsymbol{x}) = 0 \tag{B4}$$

as an approximation of $\boldsymbol{e}_c^{(1)}(\boldsymbol{x}+\boldsymbol{\Delta})\cdot\boldsymbol{a}_c(\boldsymbol{x}+\boldsymbol{\Delta}) = 0$. By substituting (B3) into (B4), we obtain

$$\boldsymbol{\Delta}\cdot\boldsymbol{e}_c^{(1)}(\boldsymbol{x}) = -\frac{\boldsymbol{e}_c^{(1)}(\boldsymbol{x})\cdot\boldsymbol{a}_c(\boldsymbol{x})}{\lambda_c^{(1)}(\boldsymbol{x})}. \tag{B5}$$

Here, we have used $\boldsymbol{e}_c^{(m)}\cdot\boldsymbol{e}_c^{(n)} = \delta_{mn}$. Since $\mathcal{A}_c$ tends to be perpendicular to $\boldsymbol{e}_c^{(1)}$ (Fig. 7), $\boldsymbol{\Delta}$ with the smallest $|\boldsymbol{\Delta}|$ can be found by imposing

$$\boldsymbol{\Delta} \parallel \boldsymbol{e}_c^{(1)}. \tag{B6}$$

Then, (B5) and (B6) lead to

$$\boldsymbol{\Delta} = -\frac{\boldsymbol{e}_c^{(1)}(\boldsymbol{x})\cdot\boldsymbol{a}_c(\boldsymbol{x})}{\lambda_c^{(1)}(\boldsymbol{x})}\boldsymbol{e}_c^{(1)}(\boldsymbol{x}). \tag{B7}$$

If we need to find more precise positions where (15) is satisfied, we may iterate the above procedure for $\boldsymbol{x}+\boldsymbol{\Delta}$ in place of $\boldsymbol{x}$. However, since the grid width $\Delta x(=2\pi/N)$ is sufficiently fine for $\boldsymbol{a}_c$, we did not iterate the procedure in the present study.

Once we find the "candidate point" $\boldsymbol{x}+\boldsymbol{\Delta}$ for each grid point $\boldsymbol{x}$, then we construct surfaces $\mathcal{A}_c$ as follows. Note that (B7) does not make sense for large $|\boldsymbol{\Delta}|$ because (B1) is a Taylor expansion. We therefore discard the candidate points which satisfy, for any i,

$$|\Delta_i| > \frac{\Delta x}{2}. \tag{B8}$$

We also discard, according to the definition (15) of $\mathcal{A}_c$, the candidate points $\boldsymbol{x}+\boldsymbol{\Delta}$ where the interpolated value of $\lambda_c^{(1)}$ is negative. Then, we use an algorithm [57] to express a surface as a set of triangles from the survived candidate points. We set the parameters of the algorithm as follows: the maximum side of triangles is $2\Delta x$ and the maximum and minimum interior angles of triangles are 120° and 10°, respectively.

[1] G. I. Taylor, Diffusion by continuous movements, Proc. London Math. Soc. **2**, 196 (1922).

[2] L. F. Richardson, Atmospheric diffusion shown on a distance-neighbour graph, Proc. R. Soc. A **110**, 709 (1926).

[3] T. Kajishima, S. Takiguchi, H. Hamasaki, and Y. Miyake, Turbulence structure of particle-laden flow in a vertical plane channel due to vortex shedding, JSME Int. J. Ser. B **44**, 526 (2001).

[4] T. Kajishima and S. Takiguchi, Interaction between particle clusters and particle-induced turbulence, Int. J. Heat Fluid Flow **23**, 639 (2002).

[5] M. Uhlmann, Interface-resolved direct numerical simulation of vertical particulate channel flow in the turbulent regime, Phys. Fluids **20**, 053305 (2008).

[6] H. Homann and J. Bec, Finite-size effects in the dynamics of neutrally buoyant particles in turbulent flow, J. Fluid Mech. **651**, 81 (2010).

[7] F. Lucci, A. Ferrante, and S. Elghobashi, Modulation of isotropic turbulence by particles of Taylor length-scale size, J. Fluid Mech. **650**, 5 (2010).

[8] H. Homann, J. Bec, and R. Grauer, Effect of turbulent fluctuations on the drag and lift forces on a towed sphere and its boundary layer, J. Fluid Mech. **721**, 155 (2013).

[9] A. G. Kidanemariam, C. Chan-Braun, T. Doychev, and M. Uhlmann, Direct numerical simulation of horizontal open channel flow with finite-size, heavy particles at low solid volume fraction, New J. Phys. **15**, 025031 (2013).
[10] M. Cisse, H. Homann, and J. Bec, Slipping motion of large neutrally buoyant particles in turbulence, J. Fluid Mech. **735**, R1 (2013).
[11] A. Chouippe and M. Uhlmann, Forcing homogeneous turbulence in direct numerical simulation of particulate flow with interface resolution and gravity, Phys. Fluids **27**, 123301 (2015).
[12] Z. Yu, Z. Lin, X. Shao, and L. P. Wang, Effects of particle-fluid density ratio on the interactions between the turbulent channel flow and finite-size particles, Phys. Rev. E **96**, 033102 (2017).
[13] M. Uhlmann and A. Chouippe, Clustering and preferential concentration of finite-size particles in forced homogeneous-isotropic turbulence, J. Fluid Mech. **812**, 991 (2017).
[14] Z. W. Lin, X. M. Shao, Z. S. Yu, and L. P. Wang, Effects of finite-size heavy particles on the turbulent flows in a square duct, J. Hydrodyn. **29**, 272 (2017).
[15] A. Chouippe and M. Uhlmann, On the influence of forced homogeneous-isotropic turbulence on the settling and clustering of finite-size particles, Acta Mech. **230**, 387 (2019).
[16] M. N. Ardekani, P. Costa, W. P. Breugem, and L. Brandt, Numerical study of the sedimentation of spheroidal particles, Int. J. Multiphase Flow **87**, 16 (2016).
[17] M. N. Ardekani, P. Costa, W. P. Breugem, F. Picano, and L. Brandt, Drag reduction in turbulent channel flow laden with finite-size oblate spheroids, J. Fluid Mech. **816**, 43 (2017).
[18] A. Eshghinejadfard, S. A. Hosseini, and D. Thévenin, Fully-resolved prolate spheroids in turbulent channel flows: A lattice Boltzmann study, AIP Adv. **7**, 095007 (2017).
[19] J. J. Derksen, Direct meso-scale simulations of fibres in turbulent liquid flow, Can. J. Chem. Eng. **88**, 677 (2010).
[20] M. Do-Quang, G. Amberg, G. Brethouwer, and A. V. Johansson, Simulation of finite-size fibers in turbulent channel flows, Phys. Rev. E **89**, 013006 (2014).
[21] M. R. Maxey, The gravitational settling of aerosol particles in homogeneous turbulence and random flow fields, J. Fluid Mech. **174**, 441 (1987).
[22] K. D. Squires and J. K. Eaton, Particle response and turbulence modification in isotropic turbulence, Phys. Fluids A **2**, 1191 (1990).
[23] K. D. Squires and J. K. Eaton, Preferential concentration of particles by turbulence, Phys. Fluids A **3**, 1169 (1991).
[24] S. Balachandar and J. K. Eaton, Turbulent dispersed multiphase flow, Annu. Rev. Fluid Mech. **42**, 111 (2010).
[25] K. Gustavsson and B. Mehlig, Statistical models for spatial patterns of heavy particles in turbulence, Adv. Phys. **65**, 1 (2016).
[26] M. Wilkinson and B. Mehlig, Caustics in turbulent aerosols, Europhys. Lett. **71**, 186 (2005).
[27] K. Gustavsson and B. Mehlig, Distribution of relative velocities in turbulent aerosols, Phys. Rev. E **84**, 045304(R) (2011).
[28] K. Gustavsson and B. Mehlig, Relative velocities of inertial particles in turbulent aerosols, J. Turbul. **15**, 34 (2014).
[29] J. Bec, Fractal clustering of inertial particles in random flows, Phys. Fluids **15**, L81 (2003).
[30] J. Bec, Multifractal concentrations of inertial particles in smooth random flows, J. Fluid Mech. **528**, 255 (2005).
[31] J. Bec, K. Gawedzki, and P. Horvai, Multifractal Clustering in Compressible Flows, Phys. Rev. Lett. **92**, 224501 (2004).
[32] L. P. Wang, A. S. Wexler, and Y. Zhou, Statistical mechanical description and modelling of turbulent collision of inertial particles, J. Fluid Mech. **415**, 117 (2000).
[33] S. Sundaram and L. R. Collins, Collision statistics in an isotropic particle-laden turbulent suspension. Part 1. Direct numerical simulations, J. Fluid Mech. **335**, 75 (1997).
[34] L. P. Wang and M. R. Maxey, Settling velocity and concentration distribution of heavy particles in homogeneous isotropic turbulence, J. Fluid Mech. **256**, 27 (1993).

[35] A. J. Petersen, L. Baker, and F. Coletti, Experimental study of inertial particles clustering and settling in homogeneous turbulence, J. Fluid Mech. **864**, 925 (2019).
[36] R. A. Shaw, Particle-turbulence interactions in atmospheric clouds, Annu. Rev. Fluid Mech. **35**, 183 (2003).
[37] P. A. Vaillancourt and M. K. Yau, Review of particle-turbulence interactions and consequences for cloud physics, Bull. Am. Met. Soc. **81**, 285 (2000).
[38] J. K. Eaton and J. R. Fessler, Preferential concentration of particles by turbulence, Int. J. Multiphase Flow **20**, 169 (1994).
[39] H. Yoshimoto and S. Goto, Self-similar clustering of inertial particles in homogeneous turbulence, J. Fluid Mech. **577**, 275 (2007).
[40] P. J. Ireland, A. D. Bragg, and L. R. Collins, The effect of Reynolds number on inertial particle dynamics in isotropic turbulence. Part 1. Simulations without gravitational effects, J. Fluid Mech. **796**, 617 (2016).
[41] A. D. Bragg, P. J. Ireland, and L. R. Collins, Mechanisms for the clustering of inertial particles in the inertial range of isotropic turbulence, Phys. Rev. E **92**, 023029 (2015).
[42] S. Goto, Y. Saito, and G. Kawahara, Hierarchy of antiparallel vortex tubes in spatially periodic turbulence at high Reynolds numbers, Phys. Rev. Fluids **2**, 064603 (2017).
[43] S. Goto and J. C. Vassilicos, Self-similar clustering of inertial particles and zero-acceleration points in fully developed two-dimensional turbulence, Phys. Fluids **18**, 115103 (2006).
[44] L. Chen, S. Goto, and J. C. Vassilicos, Turbulent clustering of stagnation points and inertial particles, J. Fluid Mech. **553**, 143 (2006).
[45] S. Goto and J. C. Vassilicos, Sweep-Stick Mechanism of Heavy Particle Clustering in Fluid Turbulence, Phys. Rev. Lett. **100**, 054503 (2008).
[46] S. W. Coleman and J. C. Vassilicos, A unified sweep-stick mechanism to explain particle clustering in two- and three-dimensional homogeneous, isotropic turbulence, Phys. Fluids **21**, 113301 (2009).
[47] M. Cencini, J. Bec, L. Biferale, Guido. Boffetta, A. Celani, A. S. Lanotte, S. Musacchio, and F. Toschi, Dynamics and statistics of heavy particles in turbulent flows, J. Turbul. **7**, N36 (2006).
[48] J. Bec, L. Biferale, G. Boffetta, A. Celani, M. Cencini, A. Lanotte, S. Musacchio, and F. Toschi, Acceleration statistics of heavy particles in turbulence, J. Fluid Mech. **550**, 349 (2006).
[49] J. Bec, L. Biferale, M. Cencini, A. Lanotte, S. Musacchio, and F. Toschi, Heavy Particle Concentration in Turbulence at Dissipative and Inertial Scales, Phys. Rev. Lett. **98**, 084502 (2007).
[50] S. Sumbekova, A. Cartellier, A. Aliseda, and M. Bourgoin, Preferential concentration of inertial sub-Kolmogorov particles: The roles of mass loading of particles, Stokes numbers, and Reynolds numbers, Phys. Rev. Fluids **2**, 024302 (2017).
[51] R. Monchaux, M. Bourgoin, and A. Cartellier, Preferential concentration of heavy particles: A Voronoï analysis, Phys. Fluids **22**, 103304 (2010).
[52] In our numerical code, we solve the equation $\partial\boldsymbol{\omega}/\partial t + \boldsymbol{u}\cdot\nabla\boldsymbol{\omega} = \boldsymbol{\omega}\cdot\nabla\boldsymbol{u} + \nu\nabla^2\boldsymbol{\omega} + \nabla\times\boldsymbol{f}$ for the vorticity $\boldsymbol{\omega}$. We impose white-in-time uniform random numbers on the Fourier modes of $\nabla\times\boldsymbol{f}^{(R)}$ in the wave-number range $k < 2$.
[53] Let us define the scale ℓ_* such that $T(\ell_*) = \tau_p$. (i) For a smaller scale ($\ell < \ell_*$), the particles with τ_p cannot follow such a rapid motion, and therefore they cannot form clusters by the action of such small-scale eddies. (ii) On the other hand, for a larger scale $\ell > \ell_*$, it is possible that the particles are swept out from the vortices of size ℓ. In such a case, we introduce $\boldsymbol{v}_c$ which is defined by (13) using $\boldsymbol{u}_c(\boldsymbol{x}, t; \ell)$. Then, the assumption (G1) is that *if the real particles in* $\boldsymbol{u}(\boldsymbol{x}, t)$ *are swept out from the eddies of size* ℓ*, then the imaginary particles in* $\boldsymbol{u}_c(\boldsymbol{x}, t; \ell)$ *are also swept out from them.* According to our understanding of the hierarchical structure of coherent vortices in developed turbulence [42], this assumption seems reasonable. Furthermore, since we now consider the case that $\ell > \ell_*$ [i.e., $T(\ell) > \tau_p$], (14) holds according to Maxey's classical argument [21].
[54] Except Figs. 5(a)–5(d), all the shown results are for the particles tracked in $\boldsymbol{u}$ without coarse-graining.
[55] H. Miura and S. Kida, Identification of tubular vortices in turbulence, J. Phys. Soc. Jpn. **66**, 1331 (1997).
[56] S. Kida and H. Miura, Swirl condition in low-pressure vortices, J. Phys. Soc. Jpn. **67**, 2166 (1998).
[57] Z. C. Marton, R. B. Rusu, and M. Beetz, On fast surface reconstruction methods for large and noisy point clouds, *2009 IEEE International Conference on Robotics and Automation* (IEEE, 2009).